Information Sciences Letters
*An International Journal*

http://dx.doi.org/10.18576/isl/121006

# Influence of Annealing Temperature on Structural, Electrical, and Magnetic Properties of $Nd_{0.7}Ca_{0.3}MnO_3$

*Sara A. Mohamed[1], I. A. Abdel-Latif[2], Ibrahim Y. Khaled[1], and Mahrous R. Ahmed[1,*]*

[1]Physics Department, Faculty of Science, Sohag University, Sohag 82524, Egypt
[2]Reactor Physics Department, Reactors Division, Nuclear Research Center, Egyptian Atomic Energy Authority, Cairo, Egypt

Received: 22 Jun. 2023, Revised: 22 Jul. 2023, Accepted: 23 Sep. 2023.
Published online: 1 Oct. 2023.

**Abstract:** In this paper, we investigated the effect of annealing temperature on the electrical and magnetic properties of polycrystalline $Nd_{0.7}Ca_{0.3}MnO_3$ synthesized using the well-known solid-state reaction technique. After the formation of the required Perovskite crystal structure phase, another annealing treatment has been done. The selected annealing temperatures are 700, 800, and 900°C for 12 hours. Structural refinement of the X-ray diffraction patterns showed the formation of a single orthorhombic crystal structure phase the of **P b n m** space group in $Nd_{0.7}Ca_{0.3}MnO_3$ without any impurity peaks. From magneto-resistance measurements, we found that NCMO samples have high-colossal magnetoresistance (CMR). Moreover, the under-investigated NCMO samples showed a high power factor. The resistivity data in the insulating region ($T > T_{MI}$) were analyzed by considering, the Mott-variable range hopping model. The phase transition temperature showed dependence on the grain size, where Curie temperature ($T_C$) increases with an increase in the grain size.

**Keywords:** Manganites; Magnetoresistance; Thermoelectric power; Magnetic properties; Crystal structure.

## 1. Introduction

Because of their unique transport and magnetic properties of rare-earth manganites, the general chemical formula $A_{1-x}B_xMnO_3$ (A= Nd, La, Pa.....& B= Ca, Sr, Ba.....) of perovskite-like structure, has recently received a lot of attention. These types of materials have different applications such as spintronics, [1,2,3] magnetic storage media, [4,5,6] magnetic sensors, [7,8,9], magnetic cooling, [10,11,12] chemical sensors, [13,14,15] and photocatalysis [16,17,18]. These compounds are promising in terms of potentially magnetic applications due to their high magnetoresistance (MR) effect, which can reach up to colossal magnetoresistance (CMR) [19,20,21,22]. B-doped compounds present an insulator-to-metal transition at a temperature TIM, tightly related to their para to ferromagnetic transition at Curie temperature $T_C$. The double-exchange model accurately describes the metallic ferromagnetic state, but in the insulator domain, where conduction is achieved by hopping of tiny polarons, polaronic effects due to high electron-phonon coupling and Jahn-Teller distortions must also be considered [23]. The orbital ordering phase [24] which is causing the lattice distortion in the manganite mother compound [25] has been studied theoretically using the anisotropic Potts model which proved the collapse happening in the unit cell [26].

The strong magnetoresistance that systems with grain boundaries present at temperatures far below the magnetic transition temperature sparked a lot of interest in polycrystalline manganites. Magnetoresistance of single crystals and epitaxial films is highest near TTM (TC) and nearly zero at low temperatures; on the other hand, polycrystalline samples have significant magnetoresistance even at low temperatures [27,28]. Grain boundaries, tunnel junctions, and grain size have all been researched extensively [29,31]. It has been demonstrated that magnetoresistance can be caused by a single boundary [32,33]. Wang et al. [34] compare the resistance with and without a 300 $mT$ magnetic field between a sample formed by conventional sintering and another acquired by "partial melting," and link the differences to "weak or strong-link grain boundaries''. Low-field magnetoresistance at low temperatures is now known to be a spin-polarized tunneling mechanism at grain boundaries [27, 35,36,37], which is linked to their half-metallic nature [38]. Through the use of low and high fields [39] or intrinsic and extrinsic components [40] to describe magnetoresistance tries to explain the observed behavior. However, some questions remain unanswered, and there is significant ambiguity regarding transportation data in these systems. While it is well known that the magnetic transition temperature is dependent on the Mn3+ content, which can be changed by modifying the oxygen stoichiometry [41], the origin of the discrepancies in the insulator to metal transition temperature for samples with the same $T_C$ is unknown. Moreover, the effect of different physical parameters on the electronic properties was investigated, for example, the effect of induced

*Corresponding author e-mail: mahrous.r.ahmed@science.sohag.edu.eg

pressure on the electronic properties of LMO compounds [42] and the annealing stage in the synthesis process plays an important role in the crystallization of any materials thus controlling their physical properties. So, in this work, we studied the influence of the annealing temperature on $Nd_{0.7}Ca_{0.3}MnO_3$ compound. We selected different temperatures 700 ºC, 800 ºC, and 900 ºC, and studied the effect of this heat treatment on the electrical, magnetic and thermoelectric power properties.

## 2. Experimental technique

$Nd_{0.7}Ca_{0.3}MnO_3$ compound (NSMO) was prepared by the conventional solid-state reaction method. The starting chemicals $Nd_2O_3$, $CaCO_3$, and $MnCO_3$ were mixed in stoichiometric proportions to prepare the NSMO structure. The raw materials were ground for 6 h and pressed into pellets at a pressure of 5-ton $cm^{-2}$. The pellet was annealed at 1173K twice for 12h in air with grounding and pressing under the same conditions. Subsequently, the pellet sintered at 1473 K for 24h in air. The obtained powder was tested by XRD to check the formation of the required NCMO phase with the well-known Perovskite-like crystal structure. The formed sample is called a green sample. The powder of the green sample was pressed to produce three pellets after that these pellets were annealed at different temperatures: at 700°C, 800°C, and 900°C for 6h.

The structural characterization was done through X-ray diffraction (XRD) with CuKα radiation at room temperature by (Bruker D8 Advance). The microstructures of samples were studied by a JSM-IT200 scanning electron microscope (SEM). The temperature dependence of resistivity was measured by a standard four-point method at zero fields and 0.6 and 1.15 Tesla in the temperature range 80-290K. The AC susceptibility of the composites was measured over the temperature range of 100K to 400K under a magnetic field of 250 μT and frequency of 0.3 kHz using the Barrington Instruments MS2/MS3. The Curie temperature, $T_C$ is determined by extrapolating the inverse susceptibility $1/\chi$ in the high-temperature range to the temperature axis, via a temperature curve.

## 3. Results and Discussion

### *3.1. Structural analysis*

XRD diffraction pattern of the green sample was taken from the angle 2θ=10° to 2q=99.987° with step 0.025631. In this range, it is seen the formation of NCMO single-crystal structure phase with the well-known Perovskite-like structure. Part of the green powder was annealed at different annealing temperatures; Tan =700°C, 800°C, and 900°C XRD patterns were measured from the angle 2q=20° to 2q=99.987°. Looking at Fig. 1, one can see the XRD patterns of green and annealed (Tan= 700, 800 & 900°C) NSMO samples. It is noted that all samples have the same crystal structure and the possible crystal symmetries were checked but the most compatible symmetry is the orthorhombic crystal symmetry [3-5, 9] Moreover, there are not any impurity peaks appearing in our case. Rietveld analysis of the experimental XRD patterns has been done using the Foolproof program and one of these patterns is shown in Fig. 2 which confirms the formation of NCMO compound in the form of orthorhombic structure with space group No 62 (**P b n m**). There is no crystal structure phase transition because of the annealing process. The refinement of the XRD pattern of NSMO@700 which is based on Rietveld is plotted in Fig.2 where the red points are the observed pattern, the black line is calculated, and the blue line is the difference between experimental and calculated. The vertical green bars are the expected Bragg's positions. The parameters resulting from the refinement for all samples are shown in table 1. The unit cell representation of both green and annealed at 700c was drawn as shown in Fig. 3 using Diamond software. The effect of the annealing and milling process is clear where the atomic position and atomic bonds are slightly changed. This change may influence the physical properties of the $Nd_{0.7}Ca_{0.3}MnO_3$ compound as we will see further in this work.

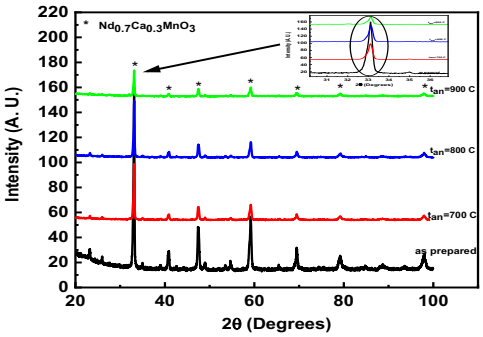


**Fig. 1:** X-ray diffraction patterns of $Nd_{0.7}Ca_{0.3}MnO_3$ green and annealed samples.

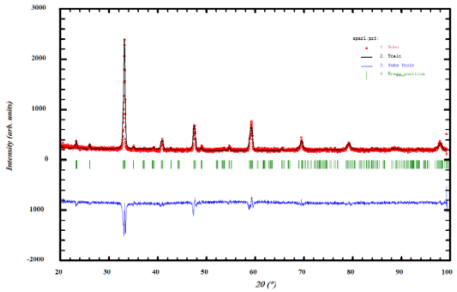

**Fig. 2:** Rietveld plot of XRD pattern of NSMO@700; red points are the observed pattern, the black line is calculated, d and the blue line is the difference between experimental and calculated. The vertical green bars are the expected Bragg's positions.

**Table 1:** Lattice parameters of NCMO with Perovskite structure of S.G. ($P_{bnm}$)

| NCMO | *Lattice parameters, Å* | | *V Å³* | *Atom* | *Atomic coordinates* | | | Bond | Angles |
|---|---|---|---|---|---|---|---|---|---|
| | | | | | *x* | *y* | *z* | | |
| Green | *a* | 5.3986 | 224.235 | Nd/Ca | -0.01609 | 0.02864 | 0.25000 | 2.08 | 159.51 |
| | *b* | 5.4449 | | Mn | 0.50000 | 0.00000 | 0.00000 | 1.83 | 124.4 |
| | *c* | 7.6284 | | $O_1$ | 0.16014 | 0.50147 | 0.25000 | | 131.3 |
| | | | | $O_2$ | -0.24421 | 0.27634 | 0.04439 | | |
| @700 | *a* | 5.3985 | 224.369 | Nd/Ca | -0.0046 | 0.0331 | 0.2500 | 1.99 | 158.5 |
| | *b* | 5.4478 | | Mn | 0.5000 | 0.0000 | 0.0000 | 1.95 | 124.2 |
| | *c* | 7.6291 | | $O_1$ | 0.0602 | 0.4696 | 0.2500 | | 130.0 |
| | | | | $O_2$ | -0.2823 | 0.2763 | 0.0503 | | |
| @800 | *a* | 5.3972 | 224.174 | Nd/Ca | -0.0054 | 0.0320 | 0.2500 | 1.99 | 160.6 |
| | *b* | 5.4467 | | Mn | 0.5000 | 0.0000 | 0.0000 | 1.93 | 126.2 |
| | *c* | 7.6258 | | $O_1$ | 0.0490 | 0.4650 | 0.2500 | | 153.9 |
| | | | | $O_2$ | -0.2823 | 0.2763 | 0.0503 | | |
| @900 | *a* | 5.3983 | 224.553 | Nd/Ca | -0.0054 | 0.0318 | 0.2500 | 1.99 | |
| | *b* | 5.4520 | | Mn | 0.5000 | 0.0000 | 0.0000 | 1.95 | 130.0 |
| | *c* | 7.6298 | | $O_1$ | 0.0379- | 0.4455 | 0.2500 | | 129.27 |
| | | | | $O_2$ | 0.2822 | 0.2763 | 0.0503 | | |

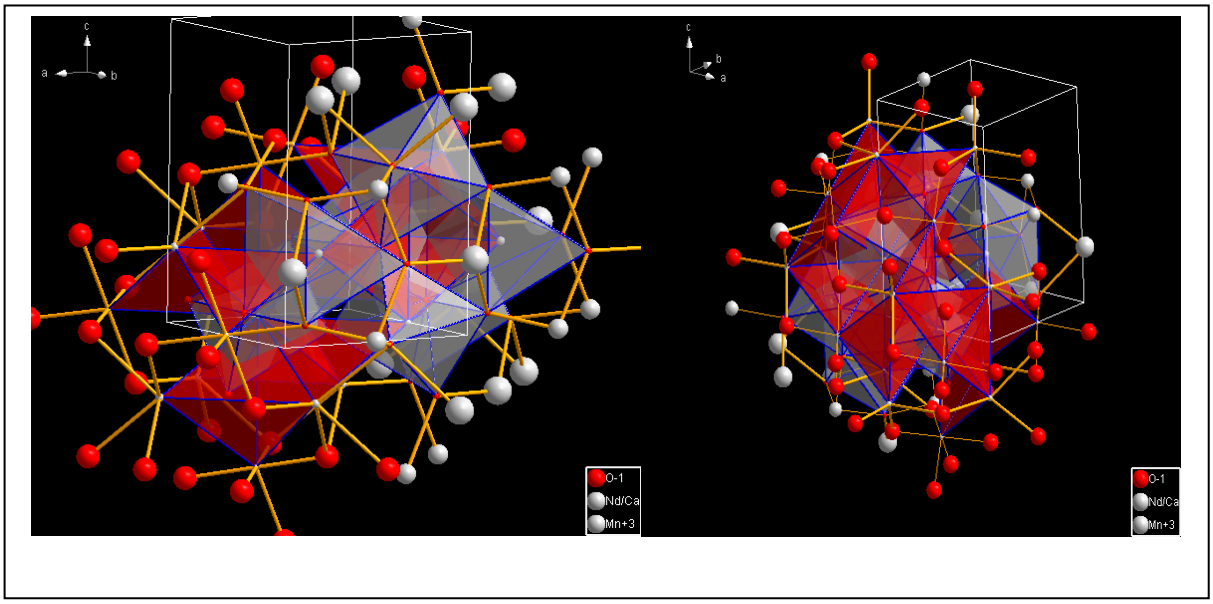


**Fig. 3:** Unit cell representation of the left-hand side green sample, and the right-hand side annealed at 700ºC sample.

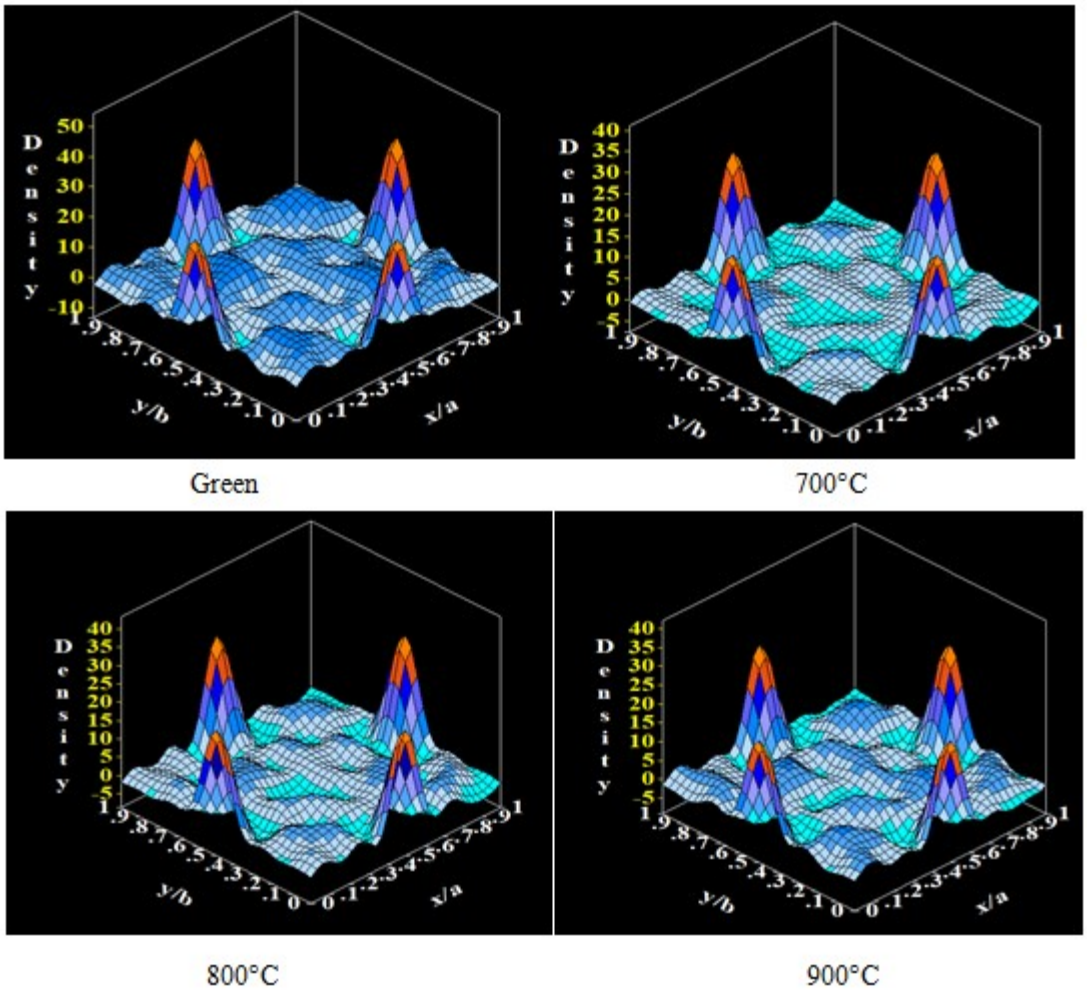


**Fig. 4:** Electronic density maps of NSMO samples from XRD.

From the broadening of the peaks corresponding to each hkl plan observed in the diffraction pattern, one can calculate the microstrain $\boldsymbol{\varepsilon=\Delta d_{hkl}/ds}$, which is established on the grains and within the grains, as seen in the XRD spectra. The $\boldsymbol{\Delta d_{hkl}}$ values are on the order of $10^{-4}$ to $10^{-3}$ nm. For the green sample the most diffraction peaks, do < ds, indicate the development of residual compressive stress on the surface, the microstrain is negative [43], but for the annealed samples do > ds, positive microstrain value indicates that the distance between the relevant crystal planes is not uniform, typically due to defects and stress, and it represents the remaining tensile stress on the particles' surfaces [44].

The electron scattering densities from the NSMO unit cell were defined in the present work using the well-known fast Fourier transform FFT as a subprogram in the Fullprof software package [45]. The electronic density has been calculated according to the following equation.

$$\rho(r) = \frac{1}{V}\sum_H F(H)\exp\{-2\pi i(H\cdot r)\}$$

where ***H, V,*** *and* ***r*** in the equation are termed to the reciprocal lattice vector, the unit cell volume, and the vector position inside the unit cell, respectively. The complex Fourier coefficients are represented by $F(\boldsymbol{H})$, which are used to perform Fourier synthesis of different types. The units of r(***r***) are associated with the unit of $F(\boldsymbol{H})$ divided by the volume. The density calculations of electrons inside the unit cell and their maps of the NSMO at different annealing temperatures are shown in Fig. 3. The difference in the electron density inside the unit cell may be attributed to the effect of annealing and milling processes which have been done for NSMO compound.

### *3.2 Scanning Electron Microscopy (SEM)*

The Scanning Electron Microscopy (SEM) micrographs and the grain size distribution histograms of prepared and annealed samples of $Nd_{0.7}Ca_{0.3}MnO_3$ are shown in Fig. 4. All samples have the same particle size distribution behavior, and they are made up of irregularly shaped grains. On the surface of the NCMO samples, grain agglomerates can be seen. Even though the green NCMO's surface is smooth, the number of grain agglomerates grows as the annealing

temperature rises, and they clash with one another. We used SEM pictures of samples to get the average grain size, GS, values. The grain size in the green sample is 1.79µm and then increases to 1.82µm as a result of annealing at temperature of $T_{an}$=700°C because this annealing modifies the surface morphology. So, we can say the increasing in the annealing temperature improves the sample's crystalline character.

On the other hand, a large number of microscopic pores emerge on the surface at temperatures Tan=800 & 900°C, where the pores size grows as a result of the annealing temperature increases. Because the grain can contain multiple agglomerated crystals, there is a significant difference between them.

### *3.3 Electrical and magnetic transport properties*

To understand the effect of annealing temperature on the electrical properties of NCMO, ρ(T) plots were recorded within the temperature range from 100 to 300 K in the presence of the magnetic field (H=0, 0.6, 1.15T) as shown in Fig 5. From this figure, it is clear that the green and the annealed sample at $T_{an}$=700°C exhibit metal-semiconducting transition at temperature $T_{ms}$ which is obtained from the inflection point green sample and $T_{an}$=700°C, ($T_{ms}$=110K), and the increase in resistivity could be due to some correlated transport and structural reasons, such as the double-exchange mechanism (DE) decreasing due to a disturbance in the $Mn^{+3}/Mn^{+4}$ ratio, oxygen-vacancy introduction [46], particle and grain size reduction (see table 1). Whereas the DE decrease in the annealed samples is due to a decrease in $Mn^{+4}$ ratio that can be affected by heat treatment [47] due to oxygen vacancies formation [46] and thus increased resistivity. In terms of structural effect, the ratio between $Mn^{+4}$ and $Mn^{+3}$ is affected by the annealing process which may lead to the Jahn–Teller active ion. In other words, this may lead to increase in distortion and give rise to increasing the value of resistivity.

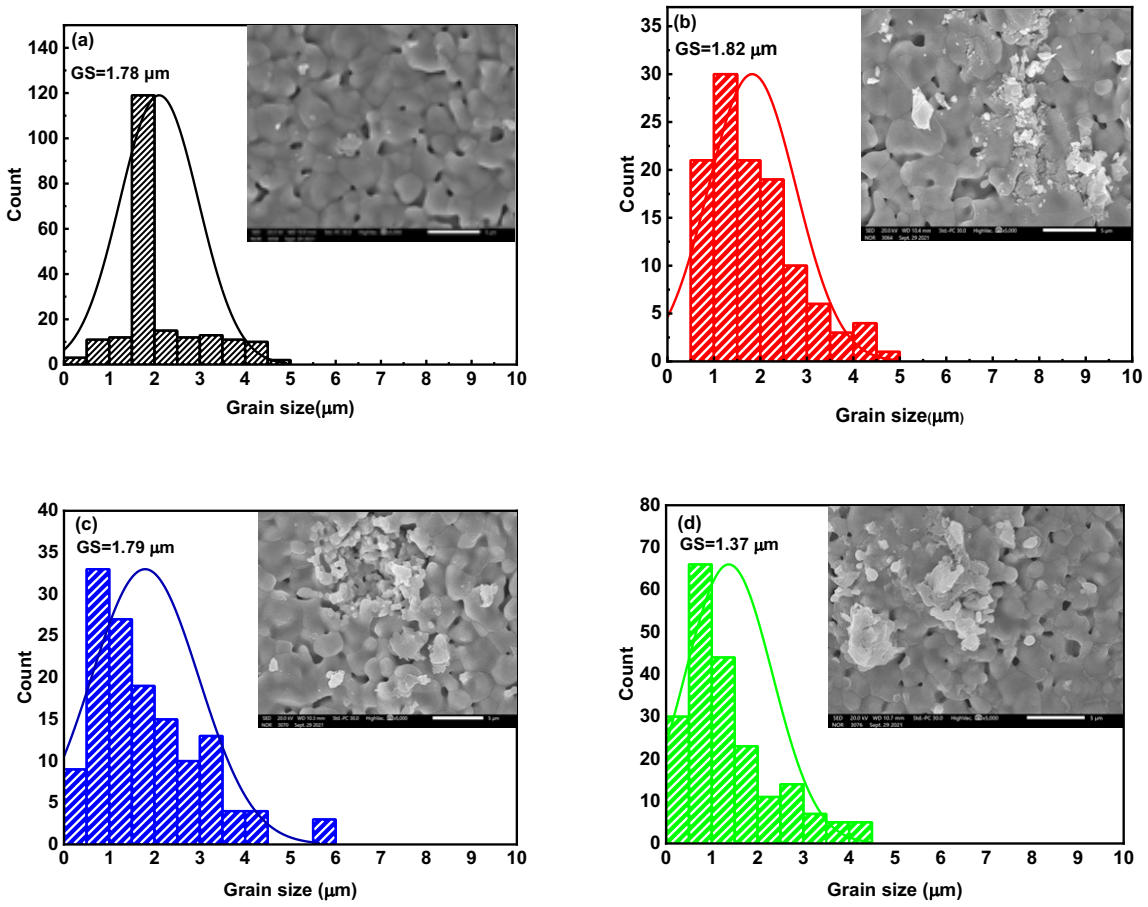


**Fig. 5:** Grain size distribution histograms and SEM micrographs for: (a)as prepared, (b) $T_{an}$=700°C, (c) $T_{an}$=800°C, (d) $T_{an}$=900°C.

Fig. 5 (a), (b) and (c) exhibit semiconductor behavior with increasing annealing temperature. The resistance drops by several orders of magnitude over a wide temperature range because of the heat treatment, which reduces the grain boundary. Besides, the heat treatment improves the connection of grain boundaries [48].

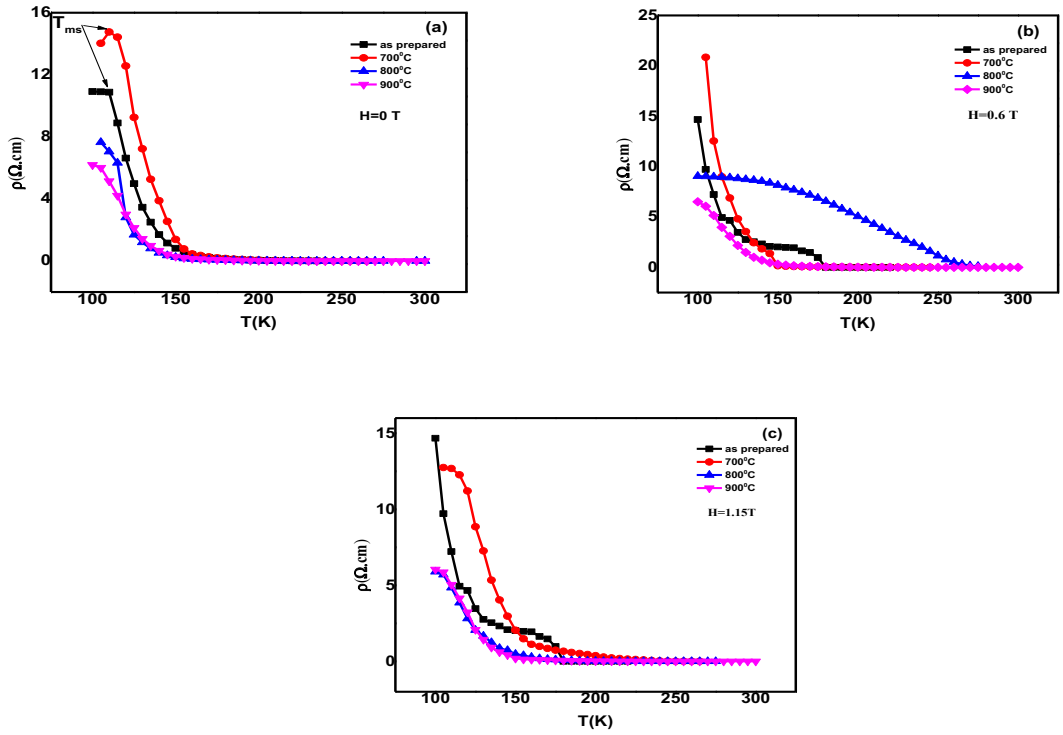


**Fig. 6:** The resistivity versus temperature of as-prepared ($Nd_{0.6}Sr_{0.4}MnO_3$) and annealed samples, (a) H=0T, (b) H=0.6T, (c) H=1.15T.

At temperatures above the transition point, the semiconducting phase can be separated into two distinct sections, each with a different mechanism. The first one is well represented by the variable range hopping (VRH) model in the range $T_{ms} \leq T \leq \Theta_{D/2}$ ($\Theta_D$ is Debye's temperature). The small polaron hopping (SPH) model matches closely with the second half (at $T \geq \Theta_{D/2}$). The temperature dependence of resistivity is described by the following equation for the VRH mechanism,

$$\sigma = \sigma_\circ \left(\frac{T_\circ}{T}\right)^{-\frac{1}{4}} \quad (1)$$

where $T_0$ is the Mott characteristic temperature and as follows:

$$T_\circ = \frac{18a^3}{k_B N(E_F)} \quad (2)$$

$N(E_F)$ is the density of states in the region of Fermi energy, and "$1/a$" is the localization length. Virt et al. [49] have reported that $a$=2.22 $nm^{-1}$. Fig. 6 shows the VRH model's experimental results for NSMO samples. Because $\Theta_D/2$ is more than $T_{ms}$, the VRH range is broad. Furthermore, $\Theta_D$ goes to a high temperature after thermal treatment of NCMO, demonstrating that the VRH range grows as the annealing temperature increases. Small polaron hopping appears in the range $T > \Theta_D/2$, where charge jumps to the nearest neighbors and hence thermally initiated hopping of small polarons dominates the conduction mechanism. The SPH model [50,51] is used to fit the data, yielding the following results:

$$\frac{\rho}{T} = \rho_\alpha \exp\left(\frac{E_\rho}{k_B T}\right) \quad (3)$$

The resistivity coefficient is determined as follows:

$$\rho_\alpha = \left[\frac{k_B}{\nu_{ph} N e^2 R^2 C(1-C)\exp(2\alpha R)}\right] \quad (4)$$

where, N is the number of ions per unit volume, R≈(1/N)1/3 is the average interest spacing, $k_B$ is the Boltzman constant, C is the fraction of sites occupied by polaron, $\nu_{ph}$ is the optical phonon frequency, and α is the electron wave function decay constant. Except for $T_{an}$=700°C, the value of υph ($h\nu_{ph}=k_B\theta_D$) for NCMO is less than $\upsilon_{ph}$ for annealed samples, showing that the frequency of lattice waves increases after thermal treatment.

The activation energy is calculated using the following equations.

$$E_\rho = W_H + \frac{W_D}{2} \quad \text{for } (T>\theta_{D/2}) \tag{5}$$

$$E_\rho = W_D \quad \text{for } (T<\theta_{D/4}) \tag{6}$$

where $W_H$ represents polaron hopping energy and $W_D$ represents disorder energy. For Tan=700°C, figure 5 shows the relationship between lin(ρ/T) and 1/T. Table 4 shows the parameters that were calculated and tabulated. The value of $E_\rho$ for $T_{an}$=700°C is less than the value of $E_\rho$ of the green sample and increases by increasing the heat treatment. The value of $E_\rho$ is inversely proportional to grain size. This means that the dependence of conduction mechanism on grain size [52]. One more parameter may affect this change in behavior is the core-shell concept provided by Zhang [53]. Increased $E_\rho$ due to oxygen deprivation may cause the Mn-O-Mn bond angle to bend, narrowing the bandwidth and increasing the effective mass of the charge carrier. As a result, the effective band gap widens as oxygen shortage increases. As a result, greater activation energies for charge carriers are required to bridge the band gap [54,55]. The (T) data were fitted to both the adiabatic and non-adiabatic polaron hopping models of $E_{min}$ and Holstein to explore the influence of annealing on polaronic transportation.

- Adiabatic polaron hopping: In this case, the relevant optical mode lattice fluctuation is long-lived compared to the electron tunneling event J>H.
- Non-adiabatic polaron hopping: In the non-adiabatic limit, the electron tunneling event is not necessarily fast compared to the relevant optical-mode lattice fluctuation J<H.

As seen in Table 2, all samples have adiabatic conduction since J>H.

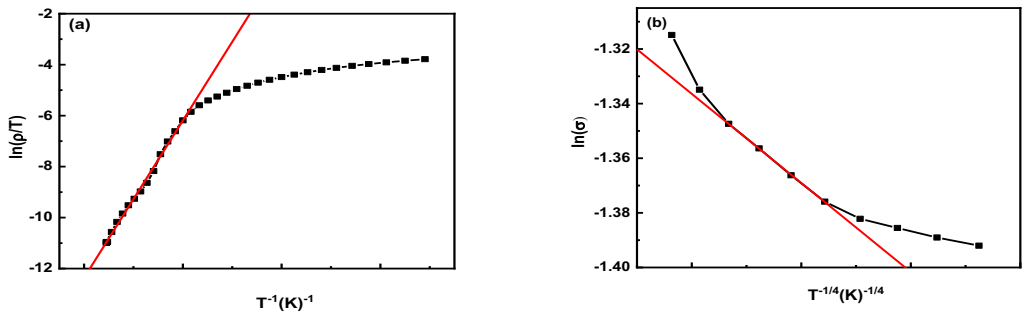


**Fig. 7:** (a) ln (ρ/T) versus 1/T and (b) ln(σ) versus $(T)^{-1/4}$ for $T_{an}$=700°C the solid line indicates the best fit to the (VRH) model between $T_{ms}$ and $\Theta_D/2$.

*3.4 Magnetoresistance*

The effect of applied magnetic fields of 0.6 and 1.15T values on the resistivity for green NSMO and annealed samples at 700ºC, 800ºC, and 900ºC temperatures have been shown in Fig. 8 (a, b, c and d). The magnetoresistance, MR, is calculated from the following equation:

$$MR = \frac{R(H)-R(0)}{R(0)}\ \% \tag{7}$$

where R(H) is the resistance with an applied magnetic field and R(0) is the resistance without a magnetic field. It can be seen that by changing the annealing temperatures enormous changes in the magnetoresistance values can be realized. As seen from Fig. 7 (a), MR of the green sample with H=0.6 T, has very small values and varies from positive to negative MR values, then increases to its maximum value of 0.07 at T=145 K, after that decreases continuously to reach its minimum value -0.14 at T=300K. But, with H=1.15 T, the variation in MR is more pronounced where it increases to its maximum value of 0.024 at T=120K, and then it decreases deeply to its minimum value of -0.21 at T=160K. MR increases again to reach a value of 0.041 at T= 200 K and then it nearly stabilizes at the end of the temperature range. MR, with H=1.14T, has negative values along the T-range because of R(0) > R(H).

**Table 2:** $T_{ms}$, $T_C$ and $E_\rho$ as a function of annealing temperature when H=0T.

| **Samples** | **Green** | **700ºC** | **800ºC** | **900ºC** |
|---|---|---|---|---|
| $T_{ms}$(K) | 110 | 110 | - | - |
| $T_C$(K) | 410 | 426 | 428 | 431 |
| $\theta_D$(K) | 260 | 250 | 310.000 | 290 |

| | | | | |
|---|---|---|---|---|
| $\nu_{ph}$(Hz)x10^12 | 5.418 | 5.209 | 6.459 | 6.043 |
| $E_\rho$(meV) | 260.358 | 240.200 | 420.458 | 398.137 |
| $W_H$(meV) | 232.727 | 226.802 | 393.821 | 370.698 |
| $W_D$(meV) | 465.453 | 453.604 | 787.642 | 741.396 |
| H(mev) | 0.145 | 0.141 | 0.181 | 0.172 |
| J(meV) | 15.427 | 14.980 | 17.602 | 16.743 |
| $\sigma_o$x10^3(mΩcm)^-1 | 1.192 | 0.001 | 65973218.810 | 408043.654 |

A colossal MR occurs when the NSMO is annealed at 700°C with H=0.6T, as shown in Fig. 8 (b), where MR has a maximum value of 2112.8% at T=235K. While with H=1.15T, MR has a very small maximum value of 3.78%, at T=155K, compared with those at H=0.6T. MR values have a positive sign with both applied magnetic fields. MR has the same behavior for both applied magnetic fields where it has positive values along the temperature range, i.e., R(H)>R(0). The increase in the MR% of the sample annealed at T=700ºC is high compared with the rest of the samples. This may be attributed to oxygen deficiency [56] and grain boundaries due to grain size reduction (spin-dependent scattering at these grain boundaries) [57] caused by spin-polarized carriers tunneling across barriers. The sample annealed at T=800ºC has opposite behaviors at both applied magnetic fields, where at H=0.6, the values of MR predominately are negative, i.e., R(0)>R (0.6), see Fig. 6(c). It decreases from a positive value of 0.49% to reach a minimum negative values-0.89% at T=150K, then it starts to increase again to -0.29%. While, at H=1.15T, the values of MR predominately are positive, i.e., R(0) < R(1.14). It starts to increase from the lowest negative value -0.09% to reach the highest positive value of 5.58% at T=215K, then it starts to decrease to reach a negative value -0.70%. This may be interpreted that the magnetic field effect overcomes the effect of the annealing process on the localization of the magnetic states at H=0.6 where the magnetic field is applied to orientation of the ferromagnetic domains so that the resistance decreases. However, at H=1.14T, the annealing process can increase the localization states which are not able to be oriented with the magnetic field. Fig. 8 (d) shows the relation between MR and T(K) of the sample annealed at Tan=900oC with an applied magnetic field H=0.6 and 1.15 T. It is seen that MR seems to have the same behavior at both the applied magnetic field and has drop points at 170K and 210K respectively, where MR values predominately are positive. The MR of polycrystalline manganites exhibits two unique patterns. Extrinsic MR arises at temperatures lower than $T_C$ with a drop in resistivity values (and consequently MR) at low applied fields, which is caused by inter-grain spin-polarized tunneling over insulating borders or spin-polarized scattering at grain boundaries induced by magnetic inhomogeneity [58,59,60]. And the intrinsic CMR response around the MI transition temperature.

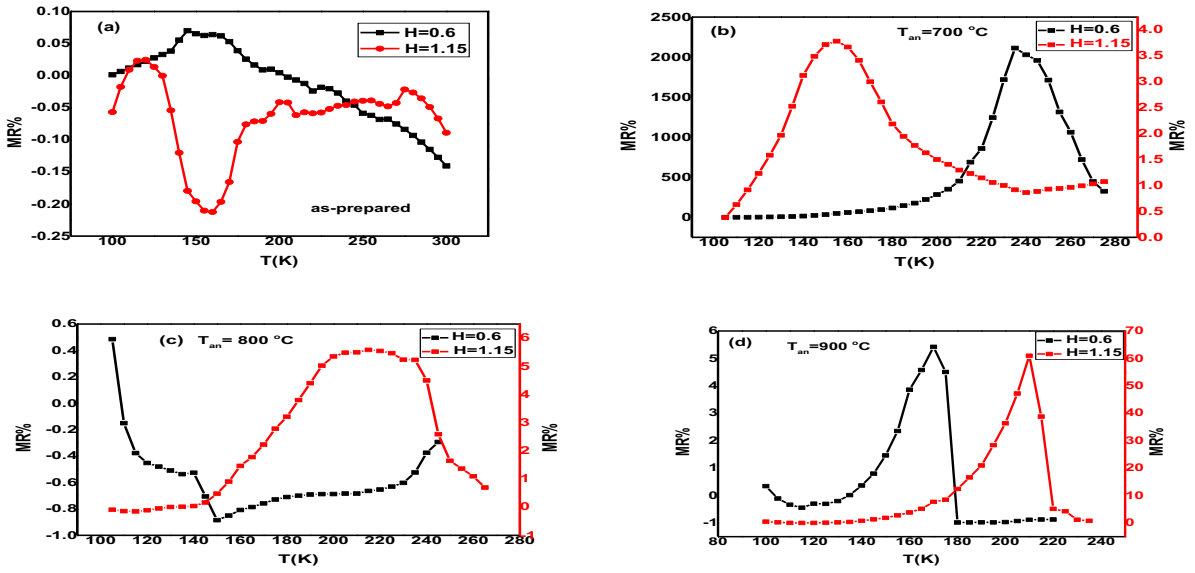


**Fig. 8:** The temperature dependence of magnetoresistance of $Nd_{0.7}Sr_{0.3}MnO_3$ at both of H=0.6T and 1.15T for the samples (a) as prepared and annealed at: (b) $T_{an}$=700ºC, (c) $T_{an}$=800ºC, (d) $T_{an}$=900ºC.

### *3.5 Specific magnetization*

The temperature dependence of magnetization was studied in zero field M(T) ZFC cooling regimes at a fixed applied magnetic field of 10 *mT* within a temperature range of 100-400 K for the green sample and annealed samples $T_{an}$=700, 800 & 900°C, see Fig. 9. The susceptibility increases steadily as the temperature decreases, peaking at Curie

temperature. The minimum of the *dM/dT* versus temperature curves is used to calculate the $T_C$ values, which are listed in Table 3. $T_C$ increases with increasing the annealing temperature. We can see the ferromagnetic transition $T_C > 400$ K. A drop in the magnetic moment indicates that the ferromagnetic order is so weak and the magnetic disorder increases. With the increase of annealing temperatures, the change in magnetization like N shape is observed. The double-exchange interaction between $Mn^{3+}$ and $Mn^{4+}$ ions causes ferromagnetic order. If the oxygen concentration is not stoichiometric, a lower $Mn^{4+}/Mn^{3+}$ ratio than the optimal value should reduce ferromagnetic order. The $Mn^{4+}/Mn^{3+}$ ratio in the NCMO bulk is increased by oxygen absorption during annealing procedures for $T_{an}$=700 & 900°C and then results in a higher ferromagnetic order but it is decreased for $T_{an}$=800°C. The increase of $T_C$ and saturation magnetization observed in the magnetic properties of our annealed NCMO samples reflected that there is an increase in the $Mn^{4+}/Mn^{3+}$ ratio due to oxygenation.

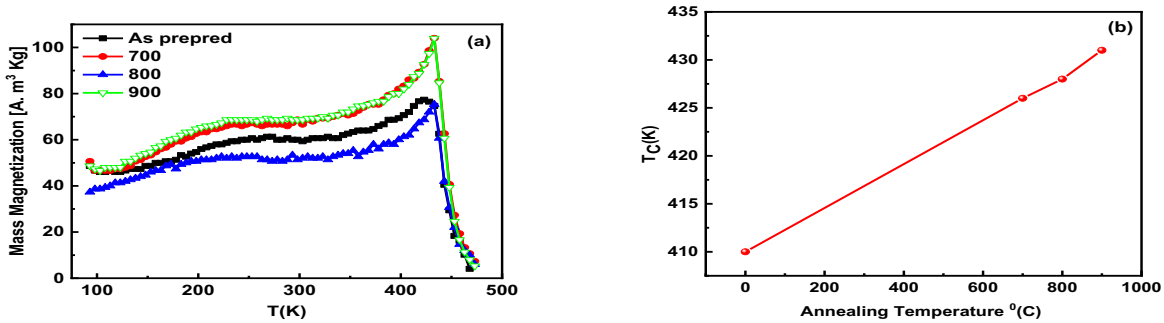


**Fig. 9:** (a) Mass magnetization of as prepared and annealing. $Nd_{0.7}Sr_{0.3}MnO_3$ samples. (b) The dependence of $T_C$ on the annealing temperature

**Table 3:** Curie temperature with annealing temperature of as prepared NCMO and annealed samples.

| **Sample** | $T_C$**(K)** |
|---|---|
| green | 410 |
| 700 | 426 |
| 800 | 428 |
| 900 | 431 |

*3.6 Thermoelectric power*

Figure 10 shows the temperature-dependent thermoelectric power of different annealed samples (green, 700, 800, 900°C). For the green sample and $T_{an}$=800°C, there are changes in the sign of the Seebeck coefficient. While for $T_{an}$=700°C the sign is negative, indicating that the sample was n-type, and finally becomes positive for $T_{an}$=900°C indicating that the dominant charge carriers were holes, throughout the temperature range of our investigation. The values of S are in the Microvolt range. All samples show a peak in S(T) at temperature ($T_S$) representing the metal-semiconductor transition and the transition temperatures ($T_S$) have an N shape, see table 4. $T_S$ expresses the T that the slope of S(1/T) changes. Several theoretical models have been proposed to analyze S for these materials at low and high-temperature ranges [61,62,63,64,65].

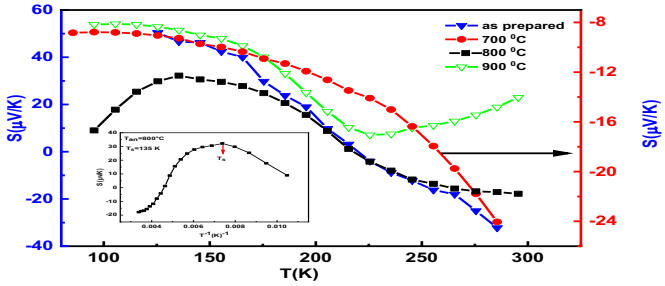


**Fig. 10:** S vs T of as-prepared NCMO and annealed samples.

Spin interactions with electrons generate magnon drag, and interactions between electrons and phonons cause phonon drag in ferromagnetic materials. The equation was used to investigate the S(T) variance below Ts [66,67] see figure 9:

$$S = S_0 + S_1T + S_{3/2}T^{3/2} + S_3T^3 + S_4T^4 \quad (8)$$

$S_0$ is a constant (S at T = 0), S1 is the diffusion coefficient; $S_3/2T_{3/2}$ term is due to the electron – magnon scattering, $S_3T^3$ is due to phonon drag and $S_4T^4$ is due to spin-wave fluctuation. Because of their low values, phonon and spin-wave fluctuation have little effect in this region, according to Table 3. Overall, this data shows that electron–magnon scattering has the most significant influence below Ts.

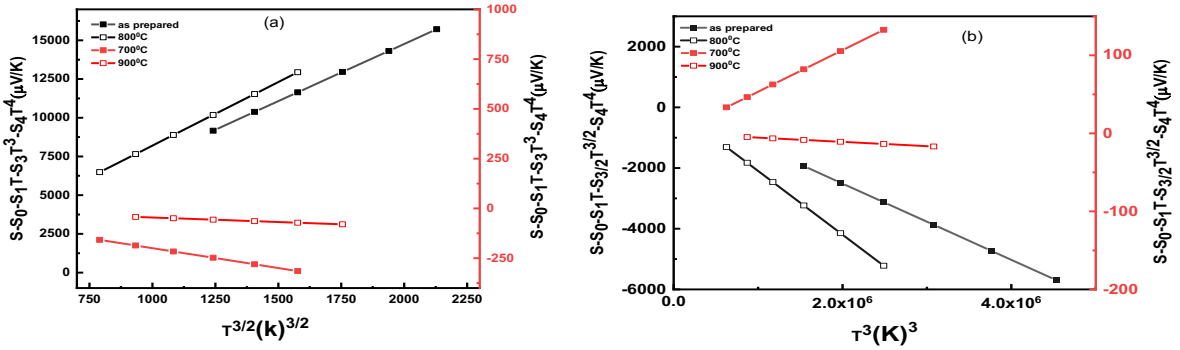


**Fig. 11:** (a) The magnon drag behavior dependent on $T^{3/2}$ & (b) The phonon drag behavior dependent on $^3$ .

**Table 4:** The parameters that best fit the thermoelectric power data for as prepared NCMO and annealed samples.

| sample | $S_0(\mu V/K)$ | $S_1(\mu V/K)$ | $S_{3/2}(\mu V/K)$ | $S_3(\mu V/K)$ | $S_4(\mu V/K)$ |
|---|---|---|---|---|---|
| **green** | 2164.26826 | -84.61935 | 7.38 | -0.00126 | 2.50E-06 |
| **700** | -45.73691 | 1.97883 | -0.19953 | 5.33122E-05 | -1.47E-07 |
| **800** | 1423.44321 | -80.44504 | 8.19959 | -0.0021 | 5.33E-06 |
| **900** | 19.30578 | 0.84995 | -0.04549 | -5.4545E-06 | 6.81E-09 |

The Mott equation was used to examine the data above Ts [68]:

$$s = {}^{K_B}/_{e}\,(E_S/K_BT + \alpha) \quad (9)$$

$E_s$ is the thermal Activation energy, and α is constant (polaron kinetic energy) [69]. The hopping is caused by a small polaron when α < 1, but it is caused by a large polaron when α > 2. As can be observed in Table 4, α < 1, which is the situation of small polaron hopping. The lower value of Es in comparison to $E_\rho$ (see table 4) derived from electrical measurements described in [70] is also interesting, indicating that SPH conduction [71] is supported.

**Table 5:** Thermopower activation energy $E_S$, the parameter α, $T_S$(,K), and the small polaron hopping energy $W_H$.

| sample | $T_S$ | $E_S$(meV) | $E_\rho$(meV) | $W_H$(meV) | A |
|---|---|---|---|---|---|
| green | 165 | 27.632 | 260.358 | 232.727 | -1444.558 |
| 700 | 235 | 13.398 | 240.200 | 226.802 | -819.121 |
| 800 | 135 | 26.637 | 420.458 | 393.821 | -1407.262 |
| 900 | 175 | 27.439 | 398.137 | 370.698 | -1343.149 |

The thermoelectric effect describes the materials ability to transform temperature differences into electrical potential. The temperature is converted to the current through the Seebeck effect[72,73,74,75]. The thermoelectric effect figure of merit equation (9) determines the thermoelectric efficiency high power factor can create more energy, which can transform some waste heat into useful electricity[76,77]:

$$z = \frac{S^2}{\rho k} \quad (10)$$

where S is the thermoelectric power, ρ is the electrical resistivity and k is the thermal conductivity. Because we didn't measure the thermal conductivity, we calculated the power factor (P) from the high value of z, low value of ρ and k, and high value of S:

$$P = \frac{S^2}{\rho} \quad (11)$$

The power factor for green and annealed samples, computed from ρ and S, is shown in Fig. 12. The power factor of both green and annealed samples increases with increasing temperatures. Annealing samples can improve the power

factor of NCMO, and our good example is annealing at 700°C has a good effect. The power factor behavior of other annealing temperatures shows the decrease in PF after annealing. All samples have a high S and P-value. P is high for $T_{an}$=700°C, especially near ambient temperature (P=594312.4 μW/cm. $K^2$). Due to the high value of S, P has a high value.

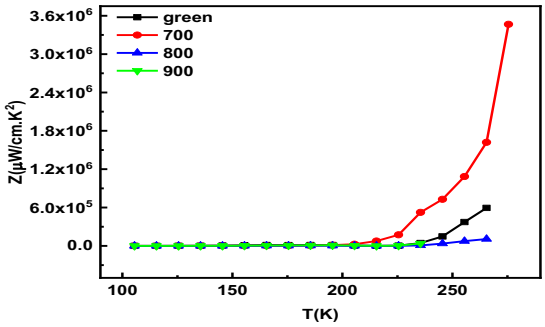


**Fig. 12:** The power factor $S^2/\rho$ of as prepared $Nd_{0.7}Ca_{0.3}MnO_3$ and annealed samples plotted as a function of the temperature

**Table 6:** Thermoelectric power factor of different oxide thermoelectric materials [78,79,80,81,82,83,84]

| Sample | T(K) | PF (μW/cm.$K^2$) | Ref |
|---|---|---|---|
| **Our samples** | | | |
| **Green** | **265** | **5.9x10$^5$** | **Present work** |
| **@700** | **275** | 5.9x10$^5$ | **Present work** |
| **@800** | **265** | 3.4x10$^6$ | **Present work** |
| **@900** | **235** | 1.2x10$^5$ | **Present work** |
| **Non Perovskite** | | | |
| **Non-Perovskite** | **300** | **83.7** | **72** |
| **$ZrTe_2$/STO** | **20** | **3x10$^5$** | **73** |
| **FeSe** | **50** | **≈13x10$^5$** | **74** |
| **$Na_xCoO_2$/Au** | **800** | **2000** | **75** |
| $BaAgCa_{2.8}Co_4O_9$ | **1000** | 3.8 x 10$^2$ | **76** |
| **Perovskite** | | | |
| $SrTi_{0.85}Nb_{0.15}O_3$ | **1220** | **35** | **77** |
| $Ca_{0.8}Lu_{0.2}MnO_3$ | 973 | 2.6 x 10$^2$ | **78** |
| $La_{0.6}K_{0.4}TiO_3$ | **720** | 6 x 10$^2$ | **79** |
| **Double Perovskite** | | | |
| $Ba_{0.15}Sr_{1.85}FeTiO_6$ | **1123** | **26** | **80** |
| $La_{0.1}Sr_{0.9}FeTiO_6$ | **1139** | **89.5** | **81** |
| $La_{0.2}Sr_{1.8}CoTiO_6$ | **1230** | **3** | **82** |
| $Sr_2TiCo_{0.5}Mo_{0.5}O_6$ | **1220** | **6.1** | **83** |
| $Sr_2TiMoO_6$ | **1220** | **7.8** | **84** |
| $Ba_2TiMoO_6$ | **1220** | **20.79** | **85** |

This means that our compounds, in particular, can be termed thermoelectric materials, especially for $T_{an}$=700°C. The power factor values for composites are comparable to the values found in other compounds as in table (5). The importance of thermoelectric power factors comes from the ability for energy conversion and the possibility of using natural energy resources. So, it is an important factor in the determination of an economic alternative route to convert solar energy into electric power.

## Conclusions

- The phase transition temperature of NCMO showed grain size dependence, where Curie temperature ($T_C$) increases with an increase in the grain size.

- The electron–magnon scattering has the most significant influence below Ts in our case.
- Due to the high value of thermoelectric power S, all samples have a high-power factor P-value which indicates that NCMO could be used as a promising candidate for green energy applications.
- The observed increase in transition temperature and saturation magnetization of our annealed NCMO samples reflects that there is an increase in the $Mn^{4+}/Mn^{3+}$ ratio due to oxygenation.
- A colossal MR was obtained for the NSMO as a result of an annealing temperature specially for $T_{an}$ = 700 °C and at a magnetic field of H=0.6T.
- The thermoelectric factors of our NCMO compound compared to other materials showed a significant advantage, allowing this compound to be used in various applications.

## Acknowledgments

The authors gratefully thank the Sohag University for supporting this work. The authors are grateful to the grant No 45643 from STDF.

## Author contributions

The authors contributions are as following: I. A. Abdel-Latif suggested the idea of the paper, Ibrahim Y. Khaled and Sara A. Mohamed execute the experimental design, where they carried out experimental measurements. Mahrous R. Ahmed did the revision of the manuscript.

## Data availability

The data of this work are available with the correspondence author.

## Conflict of interest

The authors declare that there is no conflict regarding the publication of this paper.

## References:

[1] A. I. Kurbakov, I. A. Abdel-Latif, Mahrous R. Ahmed, H. U. Habermeier, A. Al-Hajry, A. L. Malyshev, V. A. lyanov and Th. M. El-Sherbini Eur. Phys. J. Plus 137, (2022) 658.

[2] I. A. Abdel-Latif, Study on structure, electrical and dielectric properties of $Eu_{0.65}Sr_{0.35}Fe_{0.3}Mn_{0.7}O_3$, IOP Conf. Series: Mate. Sci. Eng. 146, 012003, 2016.

[3] K. Bouziane and A. Yousif, Electronic and magnetic properties of $SmFe_{1-x}Mn_xO_3$ orthoferrites (x=0.1, 0.2, and 0.3), Appl. Phys. 97, 10A504, 2005.

[4] I. A. Abdel-Latif, Crystal structure and electrical transport of nano-crystalline strontium-doped neodymium ortho-ferrites**,** J. Nanopart Res 22, 111, 2020.

[5] M. I. Irshad, F. Ahmad, N. M. Mohamed, A review on nanowires as an alternative high density magnetic storage media, *AIP Conf. Proc.* 1482, 625–632, 2012.

[6] I. A. Abdel-Latif, Study on the Effect of Nano Size of Strontium-Ytterbium Manganites on Some Physical Properties, AIP Conf. Proc. 1370, 108-115, 2011.

[7] I. A. Abdel-Latif and S. A. Saleh, Effect of iron doping on the physical properties of europium manganites, Journal of alloys and compounds, 530 (2012) 116–120.

[8] V. V. Parfenov, Sh. Sh. Bashkirov, I. A. Abdel-Latif and A. V. Marasinskaya , Transfer Phenomena in $Nd_{0.65}Sr_{0.35}Mn_{1-x}Fe_xO_3$ Ferrimanganites, Russian Physics Journal, 46, 979-983, 2003.

[9] A. A. Yousif, I. A. Abdel-Latif, K. Bouziane, A. Sellai, A. Gismelseed, I. Al-Omari, H. Widatallah, A. D. Al-Rawas, M. Elzain, Study on Mössbauer and Magnetic Properties of Strontium—Neodymium Ferrimanganites Perovskite-Like Structure, AIP Conf. Proc. 1370, 103-107, 2011.

[10] M. Kh. Hamad, I. A. Abdel-Latif and Kh A Ziq, Effect of cobalt doping in $Nd_{1-x}Sr_xMn_{1-y}Co_yO_3$, J. Phys.: Conf. Ser. 869, 012032, 2017.

[11] I. Z. Al-Yahmadi, A. Gismelssed , I. A. Abdel-Latif, F. Al Ma'Mari , A. Al-Rawas , S. Al-Harthi , I. A. Al-Omari , A. Yousf , H. Widatallah , M. ElZain , M. T. Z. Myint , properties of nanocomposites of manganite $Nd_{1-x}Sr_xMnO_3$ ($0.0 \leq x \leq 0.8$) synthesized using modified sol-gel method, Journal of Alloys and Compound, 857 (2021) 157566.

[12] M. Jeddi, J. Massoudi, H. Gharsallah, Sameh I. Ahmed, E. Dhahri and E. K. Hlil, Impact of synthesis route on structural, magnetic, magnetocaloric and critical behavior of $Nd_{0.6}Sr_{0.4}MnO_3$ manganite, RSC Adv. 11, 7238-7250, 2021.

[13] I. A. Abdel-Latif, Mohammed M. Rahman and Sher BahadarKhan, Neodymium cobalt oxide as a chemical sensor, Results in Physics, **8**, 578–.583, 2018 .

[14] S. B. Khan, M. Faisal, M. M. Rahman, I. A. Abdel-Latif, A. A. Ismail, K. Akhtar, A. Al-Hajry, A. M. Asiri and K. A. Alamry, Highly sensitive and stable phenyl-hydrazine chemical sensors based on CuO flower shapes and hollow spheres New J. Chem., **37,** 1098, 2013.

[15] Jesna George K, Vishaka V Halali, Sanjayan C. G. , V. Suvina, M. Sakar and R. Geetha Balakrishna, Perovskite nanomaterials as optical and electrochemical sensors Inorg, Chem. Front, **7**, 2702-2725, 2020.

[16] I. A. Abdel-Latif, A. A. Ismail, M. Faisal, A. M. Ali, A. Alsalmi, A. Al-Hajry, Impact of the annealing temperature on perovskite strontium doped neodymium manganites nanocomposites and their photocatalytic performances**,** Journal of the Taiwan Institute of Chemical Engineers, **75**, 174-182, 2017.

[17] Hye Ji Jang, So Jeong Park, Ju Hyun Yang, Sung-Min Hong, Choong Kyun Rhee , Dongsoo Kim, Youngku Sohn , Photocatalytic and photoelectrocatalytic properties of Eu(III)-doped perovskite $SrTiO_3$ nanoparticles with dopant level approaches, Materials Science in Semiconductor Processing, **132,** 105919, 2021.

[18] B. Barrocas, S. Sério, A. Rovisco, M.E. Melo Jorge, Visible-Light Photocatalysis in $Ca_{0.6}Ho_{0.4}MnO_3$ Films Deposited by RF-Magnetron Sputtering Using Nanosized Powder Compacted Target, J. Phys. Chem. C **118**, 590-597, 2014.

[19] Abdel-Latif, I, The particle size effect of $Yb_{0.8}R_{0.2}MnO_3$ (R is Sm, Nd, and Eu) on some physical properties, Journal of Nanoparticle Research 22, 1-12, 2020.

[20] I. A. Abdel-Latif, Mahrous R. Ahmed, I. A. Al-Omari and A. Sellai, Electrical and magnetic transport in Strontium doped Europium Ferrimanganites, Journal of Magnetism and Magnetic Materials, **420**, 363, 2016.

[21] H. Rahmouni, B. Cherif, R. Jemai, A. Dhahri and K. Khirouni, Europium substitution for lanthanium in LaBaMnO–The structural and electrical properties of $La_{0.7-x}Eu_xBa_{0.3}MnO_3$ perovskite**,** Journal of Alloys and Compound*s,* **690**, 890 – 895, 2017.

[22] Sh. Sh. Bashkirov, V. V. Parfenov, I. A. Abdel-Latif and L. D. Zaripova, Mössbauer effect and electrical properties studies of $SmFe_xMn_{1-x}O_3$ ($x$ = 0.7, 0.8 and 0.9), Journal of Alloys and Compounds, **387**, 70, 2005.

[23] A. De Andrés, M. García-Hernández and J. L. Martínez, Conduction channels and magnetoresistance in polycrystalline manganites. Phys Rev B, **60**, 7328–7334, 1999.

[24] M. R. Ahmed and G. A. Gehring, The phase diagram of an anisotropic Potts model, J. Phys. A: Math. Gen, **38**, 4047–4067, 2005.

[25] Mahrous R. Ahmed and G. A. Gehring, Potts model for the distortion transition in $LaMnO_3$, Phys Rev B, **74**, 014420, 2005.

[26] Mahrous R. Ahmed and G. A. Gehring, Volume collapse in $LaMnO_3$ studied using an anisotropic Potts model, Phys Rev B, **79**, 174106, 2009.

[27] H. Y. Hwang, S. W. Cheong, N. P. Ong, and B. Batlogg, Spin-Polarized Intergrain Tunneling in La2/3Sr1/3MnO3, Phys. Rev. Lett, 77, 2041, 1996.

[28] A. Gupta, G. Q. Gong, G. Xiao, P. R. Duncombe, P. Lecoeur, P. Trouilloud, Y. Y. Wang, V. P. Dravid, and J. Z. Sun, Phys. Rev. B, **54**, 15 629, 1996.

[29] Y. Lu, X. W. Li, G. Q. Gong, G. Xiao, A. Gupta, P. Lecoeur, J. Z. P. Sun, Y. Y. Wang, and V. P. Dravid, Large magnetotunneling effect at low magnetic fields in micrometer-scale epitaxial La0.67Sr0.33MnO3 tunnel junctions, Phys. Rev. B, **54**, 8357, 1996.

[30] M. Viret, M. Drouet, J. Nassar, J. P. Contour, C. Fermon, and A. Fert, Low-field colossal magnetoresistance in

manganite tunnel spin valves, Euro phys. Lett, **5**, 545, 1997.

[31] P. Lyu, D. Y. Xing, and J. M. Dong, Tunneling magnetoresistance in mixed-valence manganite tunnel junctions, Phys. Rev. B, **58**, 54, 1998.

[32] K. Steenbeck, T. Eick, K. Kirsch, K. Odonnell, and E. Steinbeiss, Appl. Phys. Lett, Influence of a 36.8° grain boundary on the magnetoresistance of La0.8Sr0.2MnO3−δ single crystal films, **71**, 968, 1997.

[33] N. D. Mathur, G. Burnell, S. P. Isaac, T. J. Jackson, B. S. Teo, J. L. Mac Manusdriscoll, L. F. Cohen, Large low-field magnetoresistance in $La_{0.7}Ca_{0.3}MnO_3$ induced by artificial grain boundaries, J. E. Evetts, and M. G. Blamire, Nature London, **387**, 266, 1997.

[34] X. L. Wang, S. X. Dou, H. K. Liu, M. Ionescu, and B. Zeimetz, Large low-field magnetoresistance over a wide temperature range induced by weak-link grain boundaries in La0.7Ca0.3MnO3, Appl. Phys. Lett, 73, 396, 1998.

[35] X. W. Li, A. Gupta, G. Xiao, and G. Q. Gong, Low-field magnetoresistive properties of polycrystalline and epitaxial perovskite manganite films, Appl. Phys. Lett, **71**, 1124, 1997.

[36] R. Shreekala, M. Rajeswari, K. Ghosh, A. Goyal, J. Y. Gu, C. Kwon, Z. Trajanovic, T. Boettcher, R. L. Greene, R. Ramesh, and T. Venkatesan, Effect of crystallinity on the magnetoresistance in perovskite manganese oxide thin films, Appl. Phys. Lett, **71**, 282, 1997.

[37] J. M. D. Coey, Philos. Trans. R. Soc. London, Ser. A 356, 1539, 1998.

[38] J. H. Park, E. Vescovo, H. J. Kim, C. Kwon, R. Ramesh, and I. Veukatesan, Direct evidence for a half-metallic ferromagnet , Nature, **392**, 794, 1998.

[39] Ll. Balcells, J. Fontcuberta, B. Martı´nez, and X. Obradors, High-field magnetoresistance at interfaces in manganese perovskites, P hys. Rev. B, **58**, 14 697, 1998.

[40] P. Raychaudhuri, K. Sheshadri, P. Taneja, S. Bandyopaghyay, P. Ayyub, A. K. Nigam, and R. Pinto, Spin-polarized tunneling in the half-metallic ferromagnets La0.7−xHoxSr0.3MnO3 (x=0 and 0.15): Experiment and theory, Phys. Rev. B, **59**, 13 919, 1999.

[41] H. L. Ju, J. Gopalakrishnan, J. L. Peng, Qi Li, G. C. Xiong, T. Venkatesan, and R. L. Greene, Dependence of giant magnetoresistance on oxygen stoichiometry and magnetization in polycrystalline La0.67Ba0.33MnOz, Phys. Rev. B, **51**, 6143, 1995.

[42] Saad Tariq, et al, Bandgap tuning with pressure for plausible piezoelectric and electronic applications of Lanthanum oxides LaMO3 (M = Al, Ga, Ti and V), High Temperatures-High Pressures, **51,** 179-194, 2022.

[43] Sara A Mohamed, Mahrous R Ahmed, H M Ali and A M Abdel Hakeem, Structural, electrical and optical properties investigation of nano-sized $Sb_{0.1}(SnO_2)_{0.9}$, journal of physica Scripta, **97,** 045810, 2022.

[44] A. Ayeshamariam, V. S. Vidhya, S. Sivaranjani, M. Bououdina, R. Perumal Samy, and M. Jayachandran, Synthesis and Characterizations of $SnO_2$ Nanoparticles, Journal of Nanoelectronics and Optoelectronics, **8**, 273-280, 2013.

[45] I. A. Abdel-Latif and H M Zaki, Study of structure, magnetic and electrical properties of $CoFe_{2-x}Cr_xO_4$ nanocomposites synthesized using sol-gel method, Materials Chemistry and Physics, **275**, 125256, 2022.

[46] M. Sugantha, R. S. Singh, A. Guha, A. K. Raychaudhuri, and C. N. R. Rao, Effect of substitution of $Mn^3$ by other trivalent cations on the colossal magnetoresistance and related properties of the manganates: $La_{0.7}A_{0.3}Mn_{1-x}M_xO_3$ (A = Ca, Sr, Pb; M = Al, Cr, Fe, Co), Mater. Res. Bull, **33**, 1129, 1998.

[47] A. Nossov, J. Pierre, V. Vassiliev, and V. Ustinov, Influence of annealing conditions on the magnetoresistance of (La Y Ca) manganites, Solid State Commun, **101**, 361, 1997.

[48] H. L. Ju and H. Sohn, Double exchange magnetite oxides Lal-xAxMnO3 (A= Ba, Ca), Solid State Commun, **102**, 463, 1997.

[49] M. Viret, L. Ranno, J. M. D. Coey, Magnetic localization in mixed-valence manganites, Physical Review B, **55**, 8067-8070, 1997.

[50] G. Jeffrey Snyder, R. Hiskes, S. Dicarolis, M.R. Beasley, T.H. Geballe, Intrinsic electrical transport and magnetic properties of La0.67Ca0.33MnO3 and La0.67Sr0.33MnO3 MOCVD thin films and bulk material, Phys. Rev. B **53**, 14434, 1996.

[51] M. Batlabyal, A. Ray, T. K. Deytc, Indian Journal of pure & Applied Physics 41, 443-447, 2003.

[52] G. Venkataiah, D.C. Krishna, M. Vithal, S.S. Rao, S.V. Bhat, V. Prasad, S.V. Subramanyam, P. VenugopalReddy, Effect of sintering temperature on electrical transport properties of $La_{0.67}Ca_{0.33}MnO_3$, Phys. B, **357**, 370, 2003.

[53] Zhang N., Ding W., Zhong W., Xing D., and Du Y, Tunnel-type giant magnetoresistance in the granular perovskite La0.85Sr0.15MnO3, Phys. Rev. B, **56**, 8138, 1997.

[54] Malavasi L., Mozzati M. C., Ghigna P., Azzoni C. B. and Flor G, Lattice Disorder, Electric Properties, and Magnetic Behavior of $La_{1-x}Na_xMnO_{3+\delta}$ Manganites, J. Phys. Chem. B, **107**, 2500, 2003.

[55] H. L. Ju, J. Gopalakrishnan, J. L. Peng, Q. Li, G. C. Xiong, T. Venkatesan, and R. L. Greene, Dependence of giant magnetoresistance on oxygen stoichiometry and magnetization in polycrystalline La0.67Ba0.33MnOz, Phys. Rev. B, **5**, 6143, 1995.

[56] A. J. Millis, P. B. Littlewood, and B. I. Shraiman, Double Exchange Alone Does Not Explain the Resistivity of La1−xSrxMnO3, Phys. Rev. Lett, 74, 5144, 1995.

[57] X. W. Li, A Gupta, G Xiao, and G Q Gong, Low-field magnetoresistive properties of polycrystalline and epitaxial perovskite manganite films, Appl. Phys. Lett, **71**, 1124, 1997.

[58] A. M. Haghiri-Gosnet and J P Renard, CMR manganites: physics, thin films and devices, J. Phys. D: Appl. Phys, **36**, 127, 2003.

[59] A. Gupta et al, Grain-boundary effects on the magnetoresistance properties of perovskite manganite films, Phys. Rev. B, **54**, 15629, 1996.

[60] M. F. Hundley and J. J. Neumeier, Thermoelectric power of La1−xCaxMnO3+δ: Inadequacy of the nominal Mn3+/4+valence approach, Phys. Rev. B, **55**, 11 511, 1997.

[61] A. Asamitsu, Y. Moritomo, and Y. Tokura, Thermoelectric effect in La1−xSrxMnO3, Phys. Rev. B, **53**, R2952, 1996.

[62] R. Mahendiran, S. K. Tiwary, A. K. Raychaudhurai, T. V. Ramakrishnan, R. Mahesh, N. Rangavittal, and C. N. R. Rao, Structure, electron-transport properties, and giant magnetoresistance of hole-doped LaMnO3 systems, Phys. Rev. B, **53**, 3348, 1996.

[63] R. Mahendiran, S. K. Tiwary, A. K. Raychaudhurai, R. Mahesh, and C. N. R. Rao, Temperature and doping dependence of the thermopower in LaMnO3, Phys. Rev. B **61**, 14675, 1996.

[64] I. V. H. Crespi, L. Lu, Y. X. Jia, K. Khazeni, A. Zettl, and M. L. Cohen, Thermopower of single-crystal $Nd_{1-x}(Sr,Pb)_xMnO_{3-\delta}$, Phys. Rev. B, **53**, 14 303, 1996.

[65] S. Battacharya, S. Pal, A. Banerjee, H.D. Yang, B.K. Chaudhuri, Magnetotransport properties of alkali metal doped La–Ca–Mn–O system under pulsed magnetic field: Decrease of small polaron coupling constant and melting of polarons in the high temperature phase, J. Chem. Phys, **119**, 3972, 2003.

[66] B. H. Kim, J.S. Kim, T.H. Park, D.S. Le, Y.W. Park, Magnon drag effect as the dominant contribution to the thermopower in $Bi_{0.5-x}La_xSr_{0.5}MnO_3$ ($0.1 \leq x \leq 0.4$), J. Appl. Phys, **103**, 113717, 2008.

[67] N. F. Mott and E. A. Davis, Electronic processes in non-crystalline materials, Oxford University Press, London UK, 2012.

[68] K. Sega, Y. Kuroda, and H. Sakata, D.c. conductivity of V2O5–MnO–TeO2 glasses, J. Mater. Sci, **33**, 1303, 1998.

[69] A. M. Ahmed, H. F. Mohamed, A. K. Diab, S. A. Mohamed, Synthesis, characterization and low field magnetotransport of $Nd_{0.6}Sr_{0.4}MnO_3/CrO_3$ composite, Indian J. Phys. 91 (2), 169–181, 2017.

[70] S. Battacharya, S. Pal, A. Banerjee, H.D. Yang, B.K. Chaudhuri, Magnetotransport properties of alkali metal doped La–Ca–Mn–O system under pulsed magnetic field: Decrease of small polaron coupling constant and melting of polarons in the high temperature phase, J. Chem. Phys, **119**, 3972, 2003.

[71] Zhiyi Guo, Zhiwei Wang, Shuangbin Han, Hongjian Zhao, Ying Liu, Yufu Yan, O.G. Klimova, E.S. Vasilyeva, V.E. Gasumyants, O.V. Tolochko, Puguang Ji, Fuxing Yin, Improvement of $MoS_2$ thermoelectric power factor by doping $WSe_2$ nanoparticle, Materials Today Communications, **31**, 103420, 2022.

[72] Chun Hung Suen, S. H. Cai, Hui Li, Xiaodan Tang, Huichao Wang, M. Q. He, Y. S. Chai, K. Zhou, Chi Man Wong, Jiannong Wang, X. Y. Zhou and Ji-Yan Dai, Enormous thermoelectric power factor of $ZrTe_2/SrTiO_3$

heterostructure, J. Research Square, V1, 2021, https://doi.org/10.21203/rs.3.rs-89694/v1, preprint 2021.

[73] Sunao Shimizu, Junichi Shiogai, Nayuta Takemori, Shiro Sakai, Hiroaki Ikeda, Ryotaro Arita, Tsutomu Nojima, Atsushi Tsukazaki and Yoshihiro Iwasa, Giant thermoelectric power factor in ultrathin FeSe superconductor, J. Nature communications, **10,** 825, 2019.

[74] Xiaohui Zhao, Haifeng Wang, Shufang Wang, Dogheche Elhadj, Jianglong Wangab and Guangsheng Fu, Enhancement of thermoelectric power factor in $Na_xCoO_2$/Au multilayers, J. RSC Adv, **4**, 57148, 2014.

[75] F. Zhang, Q. Lu, and J. Zhang, Synthesis and high-temperature thermoelectric properties of $Ba_xAg_yCa_{3-x-y}Co_4O_9$ compounds, J. Alloys Compd, **484**, 550, 2009.

[76] M. Saxena, K. Tanwar, and T. Maiti, Environmental friendly $Sr_2TiMoO_6$ double perovskite for high-temperature thermoelectric applications, Scr. Mater, **130**, 205, 2017.

[77] R. Funahashi, A. Kosuga, N. Miyasou, E. Takeuchi, S. Urata, K. Lee, H. Ohta, and K. Koumoto, Thermoelectric properties of $CaMnO_3$ system. In Thermoelectrics, 26th International Conference, 124, 2007

[78] L. Daniels, S. Ling, S. Savvin, M. Pitcher, M. Dyer, J. Claridge, B. Slater, F. Corà, J. Alaria, and M. Rosseinsky, A and B site doping of a phonon-glass perovskite oxide thermoelectric, J. Mater. Chem. A, **6**, 15640-15652, 2018.

[79] P. Roy, V. Waghmare, and T. Maiti, Environmentally friendly $Ba_xSr_{2-x}TiFeO_6$ double perovskite with enhanced thermopower for high-temperature thermoelectric power generation. RSC Adv, **6**, 54636, 2016.

[80] P. Roy and T. Maiti, Colossal change in thermopower with temperature-driven p–n type conduction switching in $La_xSr_{2-x}TiFeO_6$ double perovskites, J. Phys. D: Appl. Phys, **51**, 065104, 2018.

[81] T. Sugahara and M. Ohtaki, Structural and semiconductor-to metal transitions of double-perovskite cobalt oxide $Sr_{2-x}La_xCoTiO_{6-\delta}$ with enhanced thermoelectric capability, Appl. Phys. Lett, **99**, 062107, 2011.

[82] M. Saxena and T. Maiti, Compositional modification of $Sr_2TiCoO_6$ double perovskites by Mo and La for high-temperature thermoelectric applications, Ceram. Int, **44**, 2732, 2018.

[83] M. Saxena, K. Tanwar, and T. Maiti, Environmental friendly $Sr_2TiMoO_6$ double perovskite for high-temperature thermoelectric applications, Scr. Mater, **130**, 205, 2017.

[84] M. Saxena and T. Maiti, Effect of Ba-doping on high-temperature thermoelectric properties of $Sr_2TiMoO_6$ double perovskites, J. Alloys Compd, **710**, 472, 2017.